Journal of Solid State Electrochemistry
https://doi.org/10.1007/s10008-020-04837-2

ORIGINAL PAPER

Single and ternary nanocomposite electrodes of Mn_3O_4/TiO_2/rGO for supercapacitors

M. El-Shahat[1] · M. Mochtar[1] · M. M. Rashad[2] · M. A. Mousa[1]

Received: 23 June 2020 / Revised: 6 September 2020 / Accepted: 4 October 2020

Abstract

Graphene (G) and ternary nanocomposites of Mn_3O_4, TiO_2, and reduced graphene oxide(rGO) electrodes have been prepared for supercapacitor applications. The as-synthesized samples were characterized using several techniques including XRD, SEM, TEM, XPS, and Raman spectroscopy. Electrochemical characterizations were studied via cyclic voltammetry (CV), galvanostatic charge–discharge (GCD), and electrochemical impedance spectroscopy (EIS). XRD patterns of TiO_2 and Mn_3O_4 showed the formation of anatase and hausmannite tetragonal nanoparticles, respectively, whereas rGO and G showed an amorphous structure. The TEM analysis showed spherical shaped particles with less than 50 nm sizes for Mn_3O_4, nanotube for TiO_2, fiber structure for rGO, and layered structure for graphene. The Mn_3O_4/TiO_2/rGO ternary nanocomposite electrode presented a much higher specific capacitance than its single individual constituents. The ternary nanocomposite has a specific capacitance of 356 F g^{-1} in 6 M KOH aqueous electrolyte and respectable cycling performance, with 91% capacitance retained over 3000 cycles referring to its suitability for supercapacitor applications. An asymmetric supercapacitor (ASC) was constructed using a Mn_3O_4–TiO_2–rGO (MTrGO) as a positive electrode and G as a negative electrode. The organized (ASC) works steadily under the potential window of 0–1.8 V and provides a high-energy density of 31.95 Wh kg^{-1} at a power density of 7188 W kg^{-1} complemented by satisfactory cycle stability with 87% capacitance retention over 1000 cycles.

Keywords Mn_3O_4/TiO_2/rGO nanocomposite · Cyclic voltammetry · Galvanostatic charge–discharge impedance spectroscopy · Asymmetric supercapacitor

Highlights

- The Mn_3O_4/TiO_2/reduced graphene oxide nanocomposite was synthesized using a hydrothermal method.
- Nanotube TiO_2 and spherical Mn_3O_4 nanoparticles were well-dispersed on reduced graphene oxide.
- The Mn_3O_4/TiO_2/rGO ternary nanocomposite electrode showed a much higher specific capacitance than its single individual constituents.
- An asymmetric supercapacitor (ASC) constructed using a Mn_3O_4–TiO_2–rGO (MTrGO) as a positive electrode and G as a negative electrode works steadily under a potential window of 0–1.8 V providing a high-energy density of 31.95 Wh kg^{-1} at a power density of 7188 W kg^{-1} in 6 M KOH aqueous electrolyte.
- The ASC exhibits satisfactory cycle stability with 87% capacitance retention over 1000 cycles.

✉ M. A. Mousa
mousa_chem@yahoo.com

[1] Chemistry Department, Faculty of Science, Benha University, Benha, Egypt

[2] Central Metallurgical Research and Development Institute, Cairo, Helwan, Egypt

Introduction

With the fast growth of the economy, the consumption, and the diminishing supply of traditional fossil fuels, and with rising expanding global warming conditions and the increasing environmental pollution, there is a demanding requirement of looking for clean and renewable energy sources, besides highly efficient and low-cost energy storage technologies. The electrochemical energy conversion and applications as well as its compatibility with power generation from solar, wind, and nuclear resources are considered as one of the mounting interests in the improvement of low-cost, high-power electrochemical energy storage devices [1, 2]. With the developments of technology, several classes of valuable technologies for energy storage have been researched, such as batteries, fuel cells, capacitors, and supercapacitors. The capacitors and batteries as types of energy storage are limited by the low-energy density and slow power output, respectively, whereas the supercapacitors, as a new type of energy storage elements, have a large capacity, robust lifetimes, wide

Published online: 10 November 2020

working temperature range, high dynamic charge propagation, rapid charging capabilities, and low cost [3–8]. There are two kinds of supercapacitors, double-layer capacitors (EDLCs), and pseudocapacitors (or redox supercapacitors). They are differentiated by their charge storage mechanisms. The first class is based on electrostatic charge storage at the interface between electrode and electrolyte, which are frequently made of carbon-based materials. The second class of supercapacitors depends on a fast and reversible redox reaction to store charge and is usually noticeable in transition metal oxides and conducting polymers [9, 10]. Generally, supercapacitors in pseudocapacitance mode offer higher energy density than those in double-layer capacitance mode because a greater amount of charge is transported in the faradaic process in pseudocapacitance mode. Atypically, this charge transfer process produces physical and chemical modifications throughout the continued charge–discharge process, consequently decreasing their durability as compared with the supercapacitors in double-layer capacitance mode.

Nowadays, materials containing metals with different oxidation states are broadly employed as electrode materials for pseudocapacitors [2, 5–7]. In the middle of these transition metal oxides, RuO_2 holds a high specific capacitance of 720 F g^{-1} [11]. Despite this, it has not been as much consideration because of its high price and poisonousness [12]. Therefore, in the present time, the manganese oxide–based electrode materials, which are cheap and have various crystallographic structures and several oxidation states as well as an environmentally friendly nature, were used to replace the RuO_2 for supercapacitor applications [2, 13]. Mn_3O_4 as one of the manganese oxide materials has a single hausmannite structure at room temperature and considered as one of the hopeful electrode materials owing to its environment-friendly nature, low cost, good stability, and high theoretical specific capacitance (~ 1400 F g^{-1}) [13]. But the application of Mn_3O_4-based electrodes in high power supercapacitors faces restrictions because of its low electrical conductivity (~ 10^{-7}–10^{-8} S cm^{-1}) [14]. TiO_2 is also an interesting electrode material for electrochemical energy storage systems due to its perfect double-layer capacitive response and its inexpensive, naturally abundant, and environmentally safe properties [15–17]. The main challenge of using TiO_2 as an electrode material is the relatively low theoretical capacity that limits advanced practical applications due to its wide electronic band gap (~ 3.2 eV) and its high resistivity that directs to the strong internal resistance of the charge storage devices. In the present work, we fabricate TiO_2 in the morphological structure of nanotubes to overcome their high resistivity and harvest high charge storage accumulation for energy storage applications.

Several researchers attempted to increase the electrical conductivity of Mn_3O_4 and TiO_2 to be respectable for electrochemical operation [18, 19]. This can be done by making nanocomposites with highly conducting carbon nanostructures like carbon nanotubes, reduced graphene oxide, and graphene. Among the carbonaceous materials, reduced graphene oxide (rGO) is one of the best choices for supercapacitor applications due to its advantageous properties, including porous structure with mesopores and micropores, high surface area, high electrical conductivity, and good electrochemical stability [20]. Thus, by using the advantages of the properties of carbonaceous materials as well as the metal oxides with different valence states, supercapacitors with high capacitance can be constructed [21, 22].

Surface area, pore size, and size distribution play important roles in determining the solid electrodes appropriate for supercapacitor applications. The large surface area of solid materials usually has been respected as a basic directing assumption for larger capacity [23]. Above and beyond the basic prerequisite of high surface area and large pore volume, it is necessary to have a suitable pore structure for ideal supercapacitor electrode material. The nitrogen adsorption analysis is generally used to study the surface and structural properties of porous solid materials. According to IUPAC classification [24], pore size can be categorized in three classes: micropores with width < 2 nm, mesopores with width 2–50 nm, and macropores with width > 50 nm. The physical adsorption isotherms of these classes can be also classified into six types [25]. Each of these six specific types is directly linked to individual features of the pore structure and fundamental adsorption mechanism. A type I isotherm demonstrates a noticeable increase in the adsorption at low relative pressures and attains saturated adsorption, thereafter characteristic for microporous materials and monolayer adsorption on a macroporous solid. Type II or type III isotherms are characteristic for multilayer adsorption on macroporous materials. Mesoporous materials have isotherms of type IV or V [25]. In type IV, the initial part of the isotherm corresponds to the formation of mono and multilayer of adsorbate on a surface, which then is followed by instant capillary condensation in mesopores. Type V isotherms show adsorption in micro- and/or mesopores where the interactions between the adsorbent and the adsorptive are relatively weak. Isotherms of type VI are related to the adsorption on non-porous or macroporous materials. Based on the shape, the hysteresis loops in types IV and V are classified into another 4 types. In the case of type H1, the adsorption/desorption branches in the hysteresis loop are nearly vertical, which is understood to be characteristic for materials with a high degree of pore-size uniformity. Types H3 and H4 feature fairly narrow hysteresis loops, characteristic for slit-like pores, where H3 type corresponds to the aggregates of plate-like particles assembled into slit-like pores, and the H4 type is associated with highly microporous materials with slit-like pores. Mesoporous materials with numerous structural defects can also give H4 loop [26].

Herein, we report the synthesis of graphene (G) as well as single and ternary electrodes from Mn_3O_4, TiO_2, and rGO

nanomaterials using simple chemical methods. The electrochemical properties of the prepared materials as well as their uses as single and ternary composite electrodes in supercapacitors were studied. The Mn_3O_4–TiO_2–rGO (MTrGO) electrode with the highest capacitance was employed as a positive electrode for the assembling of asymmetric supercapacitor (ASC) with G as a negative electrode, and its electrochemical performances were determined using a two-electrode configuration.

Experimental

Materials

All chemicals used in this work were analytical reagents. Graphite (99.995%) was purchased from Fluke Switzerland, hydrazine monohydrate (NH_2-NH_2·H_2O) 99%, potassium permanganate ($KMnO_4$) 97%, sodium nitrate ($NaNO_3$) 95%, hydrogen peroxide (H_2O_2) 30%, ethanol (C_2H_5OH) 99%, and sulfuric acid (H_2SO_4) 98% were purchased from Adwick Pharmaceutical and Chemicals Company, Egypt.

Preparation of rGO

Graphene oxide (GO) was firstly synthesized from natural graphite matching with a modification of the Hummers–Offerman method [27]. Briefly, graphite powder (5 g) was dispersed in concentrated sulfuric acid (H_2SO_4, 115 ml, 98 wt%, in a dry ice bath). This is followed by adding 2.5 g of $NaNO_3$ into the solution. and after that, 20 g of $KMnO_4$ was gradually added with continuous strong stirring for 2 h at temperatures below 10 °C, followed by 1 h at 35 °C. Then, 250 ml of de-ionized water was inserted into the reaction in an ice bath. When the effervescence ended, we increased the temperature of the reaction to 98 °C and kept for 10 min before cooling it to room temperature. Following, 50 ml of H_2O_2 was inserted to the solution and heating to 90 °C and kept for 30 min. The produced mixture was centrifuged and washed five times with boiling water until the pH of the supernatant turns out to be neutral. Lastly, the produced solid was dried at 60 °C for 24 h. To prepare rGO, 0.1 g of the previously prepared GO was dispersed in 45 ml de-ionized water and sonicated for 25 min, following by heating to 98 °C with adding 3 ml hydrazine hydrate and keeping at 98 °C for 24 h. The rGO was then gathered by filtration and washed by distilled water five times to eliminate the excess of hydrazine, following by vacuum filtration, dried at 80 °C, and denoted as rGO.

Preparation of G

A modified chemical exfoliation method was used to prepare G from the graphite source [28]. Five grams of graphite was suspended in 100 ml of DMF for an hour; then, 0.5 mol of NaOH was added to graphite and stirred slowly for 2 h and then vigorously for 3 h. After settling the system for 1 day, G was centrifuged and washed with water until pH reaches 7 and dried at 80 °C for 1 day.

Preparation of Mn_3O_4

Mn_3O_4 was prepared by the addition of 0.02 mol $KMnO_4$ to 100 ml distilled water followed by adding 20 ml ethylene glycol with magnetically stirring for 1 h. The suspended solution was relocated to a 125-ml capacity Teflon-lined autoclave and heated under pressure to 120 °C for 4 h. The autoclave was then set aside to cool to 25 °C, and the obtained precipitate was washed five times with too much water, dried, and denoted as M.

Preparation of nanotube TiO_2

TiO_2 nanotubes were prepared by dynamic hydrothermal treatment of 3 g from commercial TiO_2 particles in 75 ml NaOH (10 M) aqueous solution in a Teflon (250 ml)-lined autoclave at 130 °C for 5 h (heating rate 2 °C min^{-1} from room temp.). The product was washed with an excess amount of de-ionized water, filtered, and washed several times until the filtrate became neutral. The produced TiO_2 was then dipped in 300 ml of 0.1 M HCl solution for 1 h, followed by filtering and washing with distilled water until pH attains 7. Lastly, the sample was dried in an oven at 95 °C for 5 h and calcined at 400 °C for 2 h and denoted as T.

Preparation of Mn_3O_4@TiO_2@rGO nanocomposite

From previously prepared reduced graphene oxide (rGO), 1.05 g was introduced to 100 ml de-ionized water and dispersed by sonication for 1 h; then, 2 g Mn_3O_4 was added to the suspension with stirring for 1 h followed by inserting 0.7 g TiO_2 and keeping stirring for 1 h. The suspended solution was then relocated to a 250-ml Teflon-lined autoclave and heated to 130 °C for 5 h. Finally, the autoclave was set aside to cool to 25 °C and the obtained precipitate was eventually washed several times with a large amount of water, dried, and denoted as MTrGO.

Characterization tools

The XRD analysis was conducted by a Philips diffractometer (Model PW-3710) using Cu Kα ($\lambda = 0.154$ nm) radiation. The diffraction patterns were collected in the 2θ range from 20 to

80°. The Raman measurements were performed by a Raman spectrometer (Renishaw brand—via Raman, with an excitation laser line of 632.8 nm from a He–Ne laser). The surface texturing properties were determined by using the N_2 adsorption isotherms technique measured at 77 K by a conventional volumetric apparatus (Quantachrome NOVA automated). The pore size distribution was decided from the desorption branch of isotherm using BJH analysis. The elemental composition was characterized by X-ray photoelectron spectroscopy (XPS; PHOIBOS 100 hemispherical analyzer, SPECS GmbH), and the excitation was Al Kα radiation at 10 kV (100 W). The survey spectra were collected with pass energy of 69 eV and the particular lines with a pass energy of 20 eV. The surface morphology and elemental analysis were done using a scanning electron microscope (SEM) Quanta FEG 250 operated at 20 kV and energy-dispersive X-ray spectrometry (EDS) EDAXTSL. Particle size and morphology were investigated by transmission electron microscope (TEM) JEOL JEM-1400.

Electrochemical measurements

Electrodes were prepared by mixing based materials with polyvinylidene fluoride (PVF) and carbon black with weight percent ratio 85:10:5, respectively, with few drops of ethanol to get a slurry form, then assembling on (FTO), and dried at 80 °C for 3 h to vaporize the solvent and achieve the best adhesion on the surface of the substrate. The electrochemical studies were carried out in three-electrode cell with the prepared active material coated on FTO glass that works as a working electrode and sheet Pt (2 cm^2) and saturated calomel electrode (SCE) as the counter and reference electrodes, respectively. A 6-M KOH aqueous solution was used as an electrolyte. The electrochemical characterization of the asymmetric supercapacitor (ASC) was performed employing the two-electrode system. PVA/KOH gel was employed as electrolyte and separator. The PVA/KOH gel electrolyte was prepared by heating 3 g of PVA powder in 50 ml of 6 M KOH aqueous solution at 85 °C for 1 h with stirring and then left to get the gelled electrolyte. The ASC was assigned by dipping the MTrGO composite as a positive electrode and G as a negative electrode into the electrolyte gel for 15 min and left to solidify. The electrodes were then dipped again in the gelled electrolyte and collected into a sandwich manner and left to solidify at 25 °C.

Results and discussions

The XRD patterns of all the investigated samples are shown in Fig. 1 and summarized in Table 1. In the case of the individual single material, the patterns of the reduced graphene oxide (rGO) show wide reflections at 2θ ~ 24° and 42° (equivalent to d spaces of 0.37 and 0.21 nm), signifying restacking to create a defectively ordered graphite-like material [29]. The XRD profile of the pure TiO_2 (T) sample displays the existence of the anatase phase with preferred orientation matches to the plane (101). All the peaks are in good agreement with JCPDS files no. 21-1272. The XRD of the Mn_3O_4 (M) powdered sample demonstrates peaks link well with the standard pattern of hausmannite tetragonal Mn_3O_4 (JCPDS 24-0734) with the space group I41/amd (JCPDS 24-0734, $a = b = 5.762$ Å, $c = 9.47$ Å). The absence of any impurity peaks, revealing the purity of the Mn_3O_4, and the fine sharp peaks verified that the prepared Mn_3O_4 particles are well crystallized. The XRD of graphene (G) shows a diffraction angle (2θ) of 26.35°, which is highly specific for the graphene sample [30]. The XRD of the ternary system Mn_3O_4@TiO_2@rGO (MTrGO) illustrates peaks match with the standard diffraction data of all the constituent materials. The peak appearing at 42.67° matching with (100) plane of rGO confirms its existence in the triple system. The intensity of XRD peaks of TiO_2 has been decreased because there are some rGO and hausmannite Mn_3O_4 coated on it. The angles of the peaks characterized for pure TiO_2 (211) and (215), as well as pure Mn_3O_4 phases (101) and (112), are slightly shifted because of the doping of each constituent into the other.

Crystallite sizes of the investigated samples ($D^{/}$) were determined using the major diffraction peaks by applying the Debye–Scherrer equation (Eq. 1) [31]:

$$D^{/} = \frac{o.9\lambda}{\beta\cos\theta} \tag{1}$$

where λ is the X-ray wavelength used and β is the half peak width of the diffraction peak. The results acquired are summarized in Table 2, and they demonstrate that the particle sizes are strongly dependent on the sample composition and lying in the range of nanometer scale.

The morphological features of the synthesized pure and composite samples were analyzed by SEM and TEM, and the images obtained are shown in Figs. 2 and 3, respectively. The SEM images of the G and rGO samples (Fig. 2a, b) and TEM (Fig. 3b, c) exhibited plates with a flake-like structure for G (Fig. 2a) and fibers with diameters of 10 nm for rGO. The SEM and TEM images of TiO_2 (Figs. 2c and 3d) show nanotubes with an average diameter and length of 5 and 150 nm, respectively. The images of Mn_3O_4 (Figs. 2d and 3e) show a mixed morphology with the majority of deformed spheres. The photographs of the ternary system MTrGO (Figs. 2e and 3f) show mixed nanoparticles of the constituent materials accompanied by a significant decrease in the fiber lengths. It could be seen that the Mn_3O_4 particles were evenly distributed on the periphery of TiO_2 and covered by the rGO nanofiber sheets.

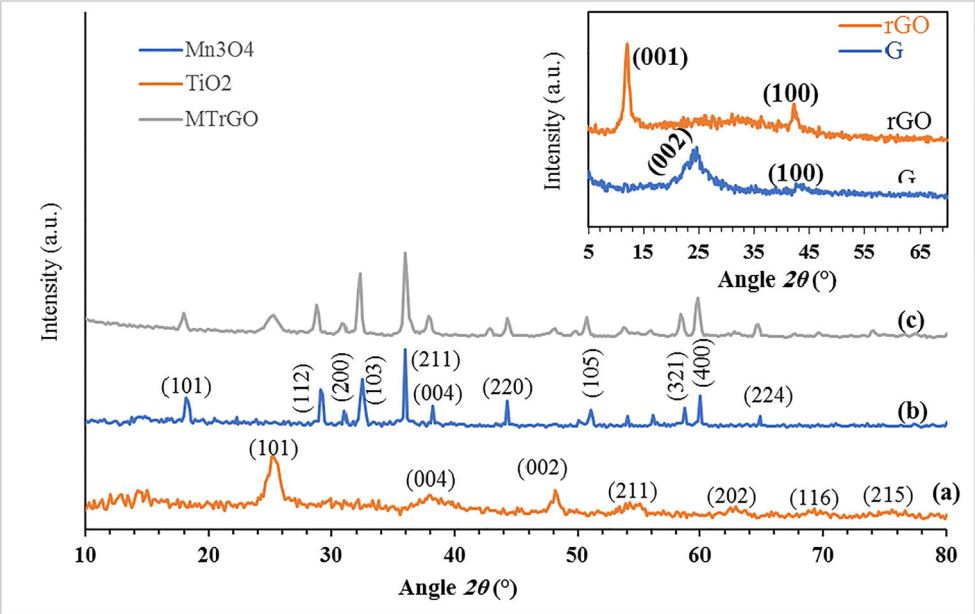

Fig. 1 XRD patterns of G, rGO, M, T, and MTrGO

The Raman spectra of rGO and MTrG nanocomposite are illustrated in Fig. 3a. It shows a characteristic peak for Mn_3O_4 at 630 cm^{-1}, in addition to two other peaks detected at ~ 1603 and 1361 cm^{-1} characterizing for the G and D bands of carbon, respectively [32, 33]. The G band is the outspread C–C stretching mode of sp^2-bonded carbon, whereas the D band is associated with the defects present in the graphene [32]. The intensity ratio (I_D/I_G) of the D and G bands can be used to qualitatively identification the defect density [33]. It should be mentioned that the D band of MTrGO composite sample is broadened and moved to 1352 cm^{-1}, and the G band is also transferred to ~ 1604 cm^{-1}, referring to the interaction occurring between rGO and the metal oxides.

For assessing the bonding configuration in all samples, X-ray photoelectron spectroscopy (XPS) studies were carried out for rGO, TiO_2, Mn_3O_4, and MTrGO samples. The XPS data of pure materials (rGO, TiO_2, and Mn_3O_4) are shown in Fig. 4 and the MTrGO composite in Fig. 5. The XPS survey spectrum of rGO shows the presence of only two elements, C and O (Fig. 4a). The deconvolutions of the C 1s peak were analyzed by curve fitting (Fig. 4b) which showed four components of the carbon bond: C–C (284.5 eV), C–O (286.5 eV), O–C=O (287.7 eV), and C=O (288.6 eV), which agree well with the literature values [34, 35]. The O 1s core-level spectra for rGO (Fig. 4c) were deconvoluted into three peaks, ascribed to quinone (530.8 eV), oxygen double-bonded to carbon (531.7 eV), and oxygen single-bonded to carbon (532.9 eV) [36, 37]. XPS spectra of pure TiO_2 are shown in Fig. 4d–f. The XPS survey spectrum of TiO_2 (Fig. 4d) shows the presence of only two elements, Ti and O. Figure 4 e shows the high-resolution XPS spectra for Ti 2p. The two strong peaks detected at binding energies of 458.48 and 464.23 eV can be assigned to Ti^{4+} $2p^{3/2}$ and Ti^{4+} $2p^{1/2}$, respectively [38]. In the O 1s spectrum (Fig. 4f), the main peak at about 530.3 eV is obtained [38]. XPS spectra of pure Mn_3O_4 are given in Fig. 4g–i. The survey XPS spectrum of Mn_3O_4 (Fig. 4g) shows

Table 1 XRD data of the investigated samples

TiO_2 (2θ)	(hkl) planes	Mn_3O_4 (2θ)	(hkl) planes	rGO (2θ)	(hkl) planes	MTrGO (2θ)	(hkl) planes	G (2θ)	(hkl) planes
25.21	(101)	17.91	(101)	24	(002)	17.97	(101)-Mn_3O_4	26.35	Amorphous
37.90	(103)	28.73	(112)	42	(100)	28.81	(112)-Mn_3O_4		
48.22	(200)	32.29	(103)			42.67	(100), rGO		
50.02	(211)	36.02	(211)			54.96	(211)-TiO_2		
62.69	(213)	44.42	(220)						
69.01	(116)	50.65	(105)						
75.06	(215)	58.42	(321)			74.94	(215)-TiO_2		
		59.81	(400)						
		64.55	(224)						

Table 2 XRD and N_2 adsorption data of the investigated samples

Sample	Particle size (nm)	Surface area (m^2 g^{-1})	Pore diameter (nm)
G	3.3	420	5.2
rGO	3.1	309.9	4.1
TiO_2	12.9	28.6	5.0
Mn_3O_4	58.9	14.4	3.9
MTrGO	35.1	55.8	7.1

only two elements O 1s (528 eV) and Mn 2p (640 eV) without any impurity. The high-resolution spectra of Mn (Fig. 4h) show the binding energy value for Mn $2p^{3/2}$ at 641.4 eV, and for Mn $2p^{1/2}$ at 653.1 eV. The spin–orbit splitting between the Mn $2p^{3/2}$ and Mn $2p^{1/2}$ levels is 11.7 eV, which agrees well with the previously reported data of Hausmannite nanoparticles [39]. In the high-resolution XPS of the O 1s (Fig. 4i), a peak located at 529.5 eV is observed, which agrees well with the literature data to oxygen in the Mn_3O_4 lattice [40].

The elemental information and the internal interaction in MTrGO composite were also explored by XPS and the data obtained are presented in Fig. 5a–e, which demonstrates the presence of all elements in spectra according to their states in the molecules. The survey XPS spectrum (Fig. 5a) of MTrGO shows the peaks of O 1s (528 eV), C 1s (284 eV), Ti (530 eV), and Mn 2p (640 eV) electrons without any impurity indicating the coexistence of O, C, Ti, and Mn elements. The investigation of carbon states (Fig. 5b) shows the presence of four types of carbon bonds, that is, C–Ti (282.1 eV), C–C (284.7 eV), C–O (287.9 eV), and COO (288.7 eV). The presence of the C–Ti bond revealed that the C atoms have substituted some of the Ti atoms in the TiO_2 lattice during the preparation. Figure 5 c shows the XPS Mn 2p spectra of the composite, in which the peaks centered at 653.5 and 641.6 eV match to Mn $2p^{1/2}$ and Mn $2p^{3/2}$ peaks. The gap between these two peaks is 11.9 eV, which agrees well with a previous report on Mn_3O_4 [41]. The spectrum of the Ti 2p band for the pure TiO_2 (Fig. 4e) is compared with that of the MTrGO composite (Fig. 5d). The gap in MTrGO between the two Ti bands was about 5.78 eV, while the gap in the pure sample was 5.71 eV. The fine particularity in the position of the two peaks may relate to the interplay between TiO_2 and the rGO, which possibly points to the existence of Ti–O–C bonds in the MTrGO nanocomposite. There is a peak associated with Ti–C bonds at about 282 eV [42] in the MTrGO samples, which denoted the carbon doping into the lattice of TiO_2. Figure 5e shows the O 1s core-level spectra of MTrGO, and all curves can be deconvoluted into three peaks as Mn–O–Mn (530.3 eV) and Mn–O–C (531.4 eV) and C–O (532.6 eV). The EDS spectrum of the ternary system was analyzed and the data is shown in Fig. 4f. It showed peaks related only to Ti, Mn, C, and O with weight percentages of 11.1%, 37.9%, 17.1%, and 33.9%, respectively. These results are consistent with the composition of the initial feeding ratios of starting materials.

Because surface and pore-size distribution are two key parameters for electroactive materials in energy conversion/storage applications [43], the N_2 adsorption analyses were carried out and the results obtained are illustrated in Fig. 6. From the figure, it is seen that all materials have hysteresis

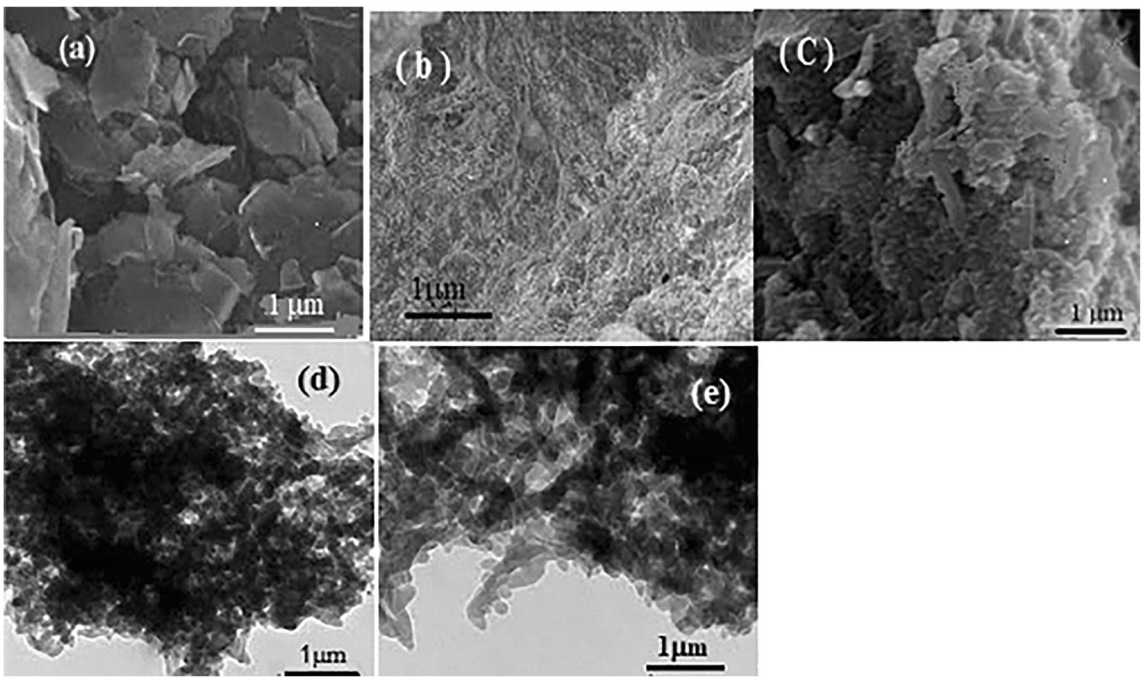

Fig. 2 SEM of the investigated samples. **a** G. **b** rGO. **c** T. **d** M. **e** MTrGO composite

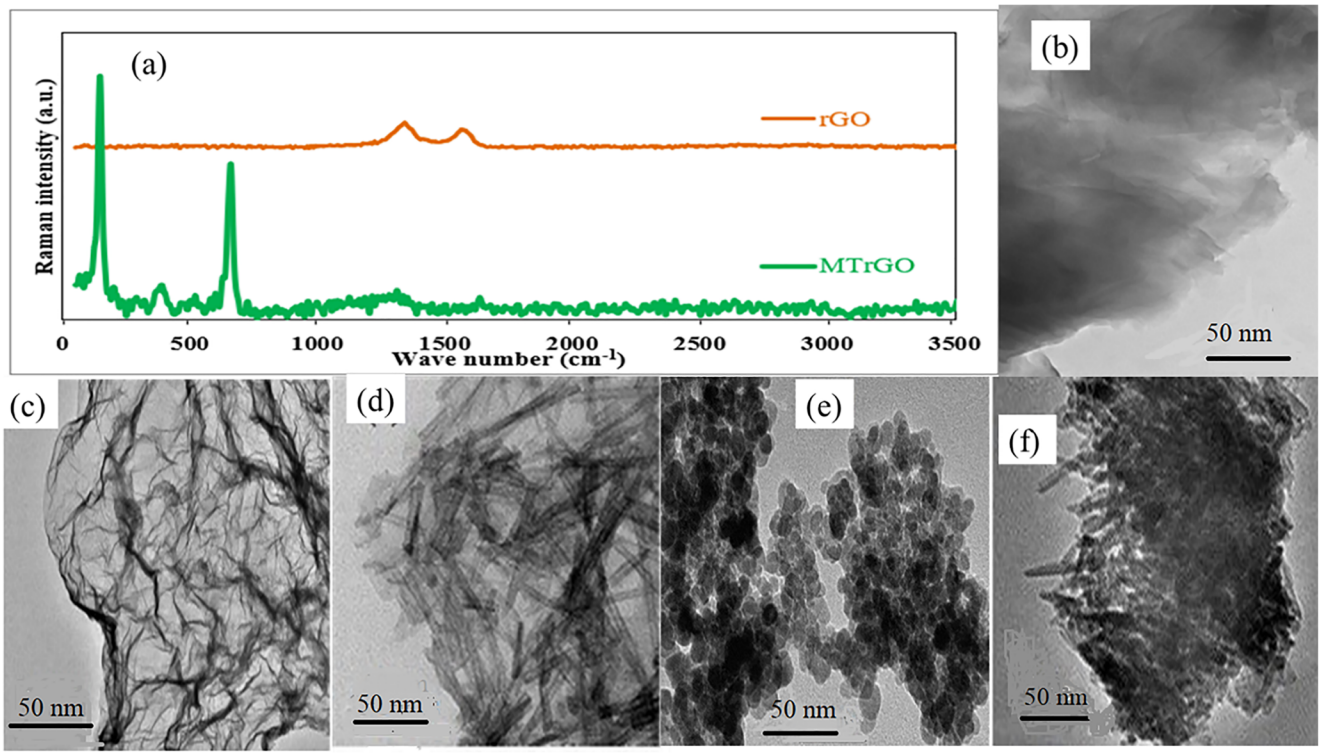

Fig. 3 **a** Raman spectra of rGO and MTrGO and TEM images of **b** G, **c** rGO, **d** T, **e** M, and **f** MTrGO samples

loops with capillary condensation ($P/P° > 0.45$) for G, rGO, and TiO_2 and ($P/P° > 0.85$) for Mn_3O_4 and MTrGO. The observed hysteresis loops of G, rGO, and TiO_2 correspond to type V with H3 charact7eristics according to the IUPAC classification and referring to the mesoporous structures, which can be attributed to a weakly interaction between the adsorbate and the adsorbent materials with the aggregates of plate-like particles assembled into slit-like pores. On the other hand, the hysteresis loops of Mn_3O_4 and MTrGO samples are better describing by the type V with H1 characteristic for a high degree of pore size uniformity. The large hysteresis loops, between the adsorption and desorption curves, of G sample, are considered to be connected either to the capillary condensation associated with large pore channels or to the modulation of the channel structure of G. The calculated specific surface area (S_{BET}) by the BET (Brunauer–Emmett–Teller) method [44] and the pore size distribution analyzed by the Barrett–Joyner–Halenda (BJH) [44] using the desorption data (given in the inset of Fig. 6) are summarized in Table 2. From which, it can be seen that the specific surface area of the studied samples increases in the following order:

$$G > rGO > MTrGO > TiO_2 > Mn_3O_4$$

Whereas the pore size diameter increases according to the following:

$$MTrGO > G > TiO_2 > rGO > Mn_3O_4$$

Electrochemical properties of positive electrodes

Figure 7 a shows the CV curves of all investigated samples recorded in 6 M KOH electrolyte at a scan rate of 10 mV s^{-1}. The CV voltammograms of TiO_2 show an almost rectangular shape referring to a dielectric behavior, whereas the CV curve of the pure Mn_3O_4 shows a pair of redox peaks. These peaks reveal to the presence of a reversible redox reaction, proposing a pseudocapacitance manner that produced from the reduction–oxidation switches of interfacial oxidation species at numerous Mn oxidation states (i.e., Mn^{2+} and Mn^{3+}). The specific capacitances (C_{sp}) were evaluated from CV voltammograms using the following equation [45].

$$C_{sp} = \frac{\int i dV}{2mv\Delta V} \quad (2)$$

where i is the current, ΔV is the potential window, m is the loading mass of the active material, and ν is the potential scan rate. The obtained results are given in Table 3, which shows that the C_{sp} of ternary material is higher than that of the individual single material.

The CV of the rGO, TiO_2, Mn_3O_4, and MTrGO are investigated at various scan rates, and the voltammograms obtained are represented in Fig. 7b–e. It can be seen that, as expected, the currents obtained increase with the increase in scan rate [46]. However, the capacitance values were found to reduce with increasing the scan rate, because of the diffusion

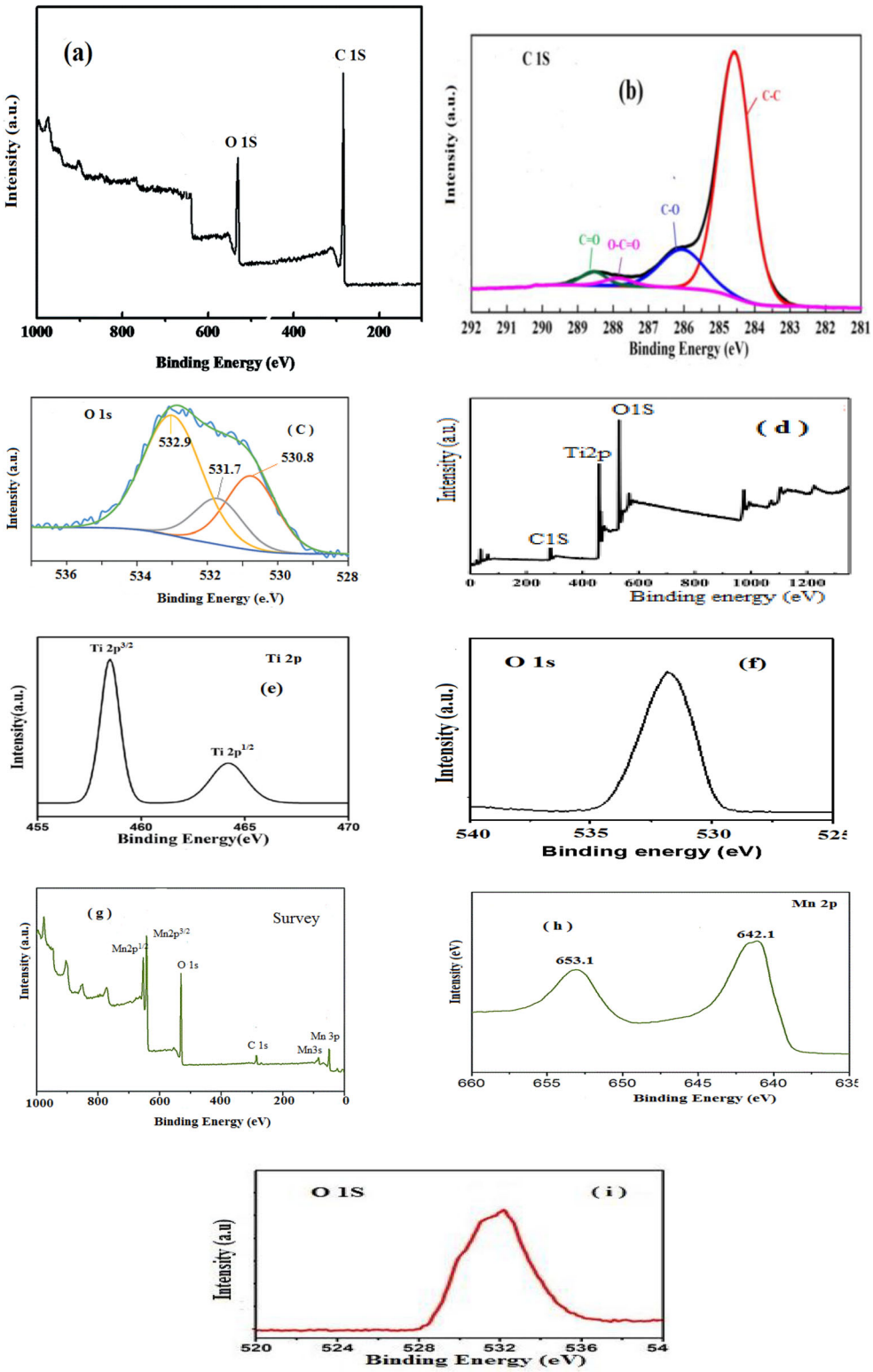

Fig. 4 XPS of **a** survey spectrum rGO, **b** high-resolution C 1s of rGO, **c** high-resolution O 1s of rGO, **d** survey spectrum TiO_2, **e** high-resolution Ti 2p of TiO_2, **f** high-resolution O 1s of TiO_2, **g** survey spectrum Mn_3O_4, **h** high-resolution Mn 2p of Mn_3O_4, and **i** high-resolution O 1s of Mn_3O_4

restrictions in the surface pores of electrodes. At the lower scan rate, the K^+ ions of the aqueous electrolyte can use all the presented locations in the active electrode material, for the reason that the K^+ has sufficient time to diffuse into all the places causing higher capacitance. Conversely, at the high-scan rate, the K^+ ions face the problem to get into all the accessible sites in the active electrode because of their limited rate of progress in the electrolyte. The

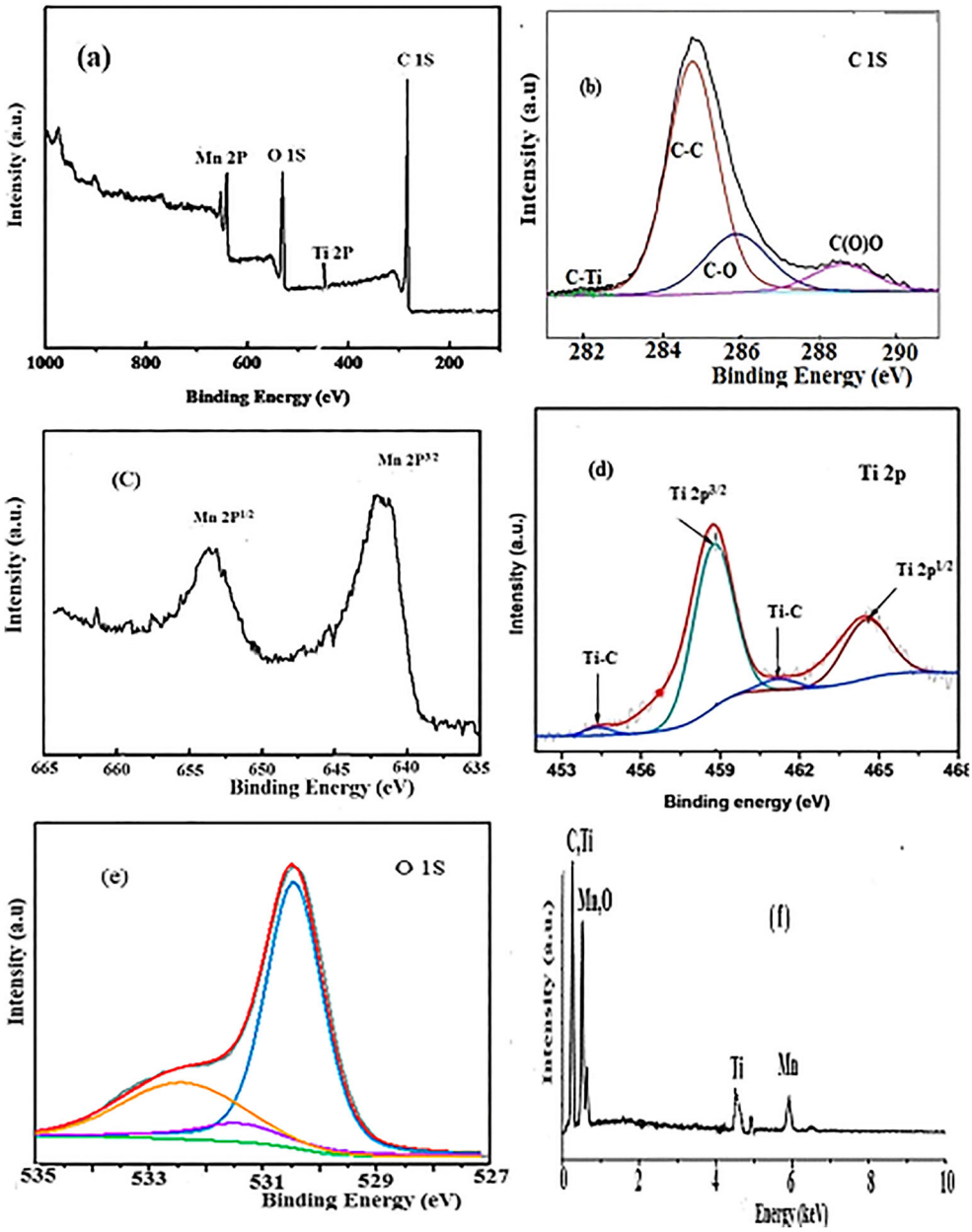

Fig. 5 XPS spectra of MTrGO composite. **a** Survey spectrum. **b** High-resolution C 1s. **c** High-resolution Mn 2p. **d** High-resolution Ti 2p. **e** High-resolution O 1s. **f** EDX data

mechanism of Mn_3O_4 electrode capacitance can be elucidated using the following relations [47]:

$$3Mn\,(OH)_2 + 2OH^- \leftrightarrow Mn_3O_4.2H_2O + 2e^- + 2H_2O \quad (3)$$

$$Mn_3O_4 \cdot 2H_2O + OH^- \leftrightarrow 2MnOOH + Mn\,(OH)_3 + e^- \quad (4)$$

The CV curves of rGO and TiO_2 (Fig. 7b, c) show nearly rectangular cyclic voltammograms, which stands out as a sign of an EDL supercapacitor. Inspection CV curves of Mn_3O_4 (Fig. 7d) show that still at a superior scan rate of 40 mV s^{-1}, the CV voltammogram of Mn_3O_4 electrode keeps its trend that exposes the improved electrochemical reversibility of the faradic redox process of the Mn_3O_4 electrode. Moreover, a perfect capacitive trend is marked by the growth in redox current concerning the scan sweep that also confirms the satisfactory rate ability of as prepared Mn_3O_4 material [48]. Our results also showed negative and positive shifts in the redox peaks by raising the scan rate [49].

The capacitance value, obtained for rGO in the present work at a scan rate of 1 mV s^{-1} (52.8 F g^{-1}), is higher than that reported by Du et al. [50]. The rGO electrode demonstrated rapid charge storage and transportation kinetics confirming by its rectangle shape and clear passing replies at both tips of the CV curve. The mesoporous structure of the surface, high electrical conductivity, and electrolyte accessibility of rGO are accountable for the performed high-rate capability.

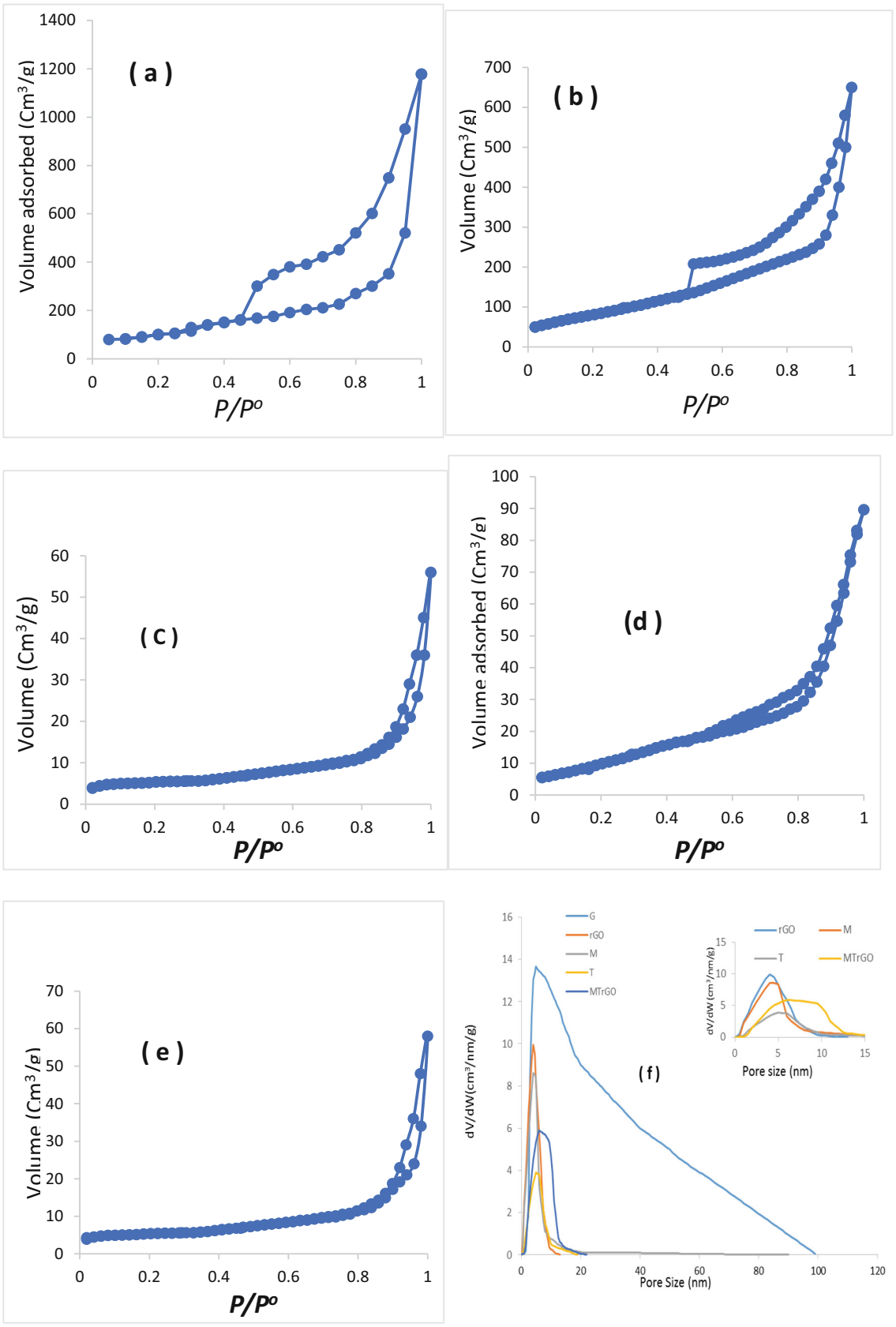

Fig. 6 BET measurement curves of all investigated samples. **a** G. **b** rGO. **c** M. **d** T. **e** MTrGO. **f** Pore size distribution

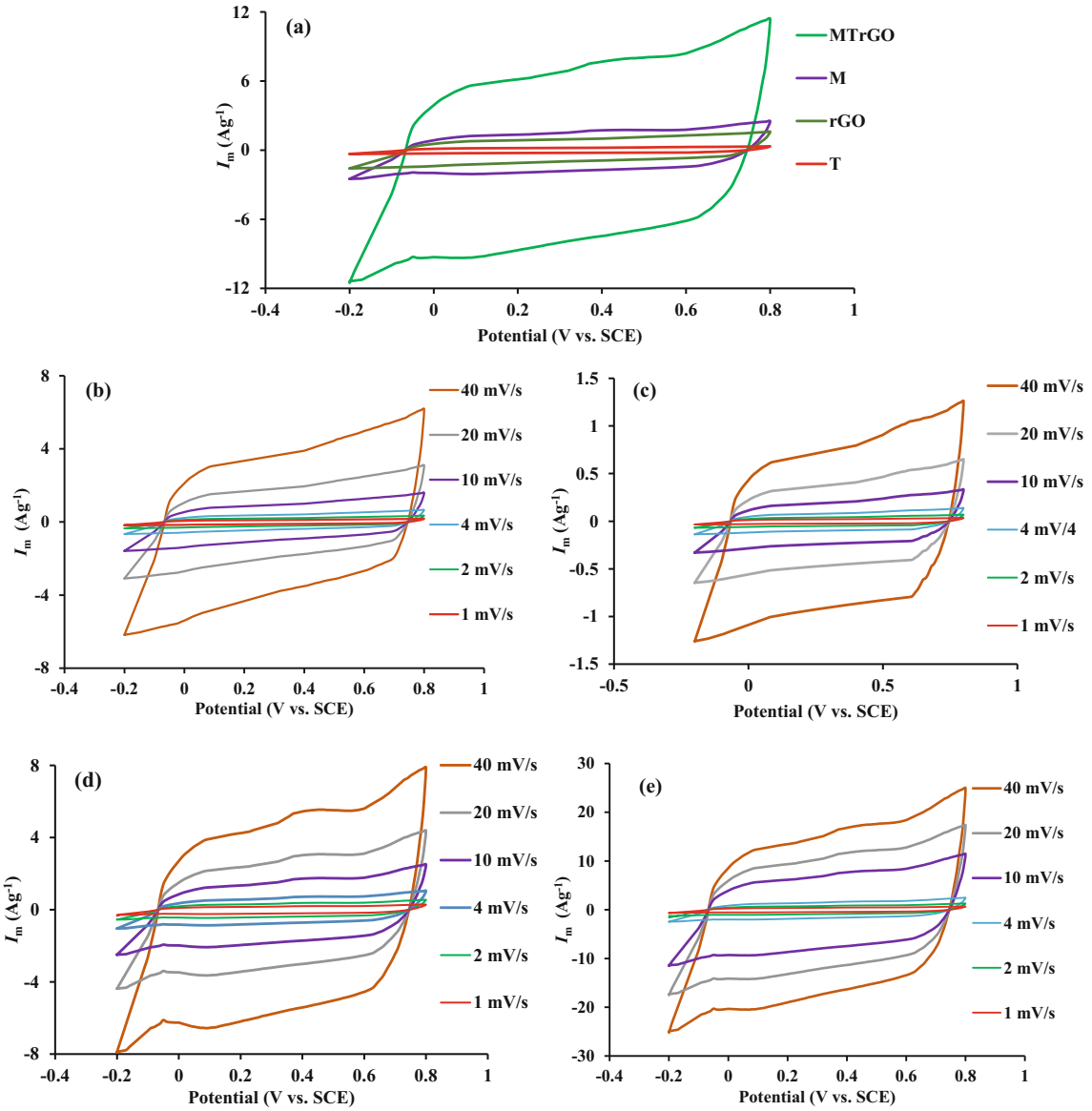

Fig. 7 Electrochemical performance of the samples measured in 6 M KOH solution. **a** CV curves of rGO, T, M, and MTrGO at a scan rate 10 mV s^{-1}. **b**–**e** CV curves of rGO, T, M, and MTrGO, respectively, at several scan rates

The CV curves of the MTrGO electrode (shown in Fig. 7e) illustrate poor symmetry with minor redox peaks, which include both surface adsorption and incorporation of the cations of electrolyte [51].

Table 3 Specific capacitance values of Mn_3O_4, TiO_2, rGO, and MTG electrodes in 6 M KOH at different CV scan rates and different discharging current densities

Sample	C_{sp} (F g^{-1}) at different scan rates (mV s^{-1})						C_{sp} (F g^{-1}) at different I_d (A g^{-1})				
	1.0	2.0	4.0	10.0	20.0	40.0	1.0	2.0	3.0	5.0	8.0
M	130	122	120	112	98	88	139.0	137.0	131.0	129.0	122.0
T	19.5	18.0	17.7	17.0	16.3	14.5	16.1	15.9	14.8	14.3	13.9
rGO	78.1	77.2	71.1	67.9	66.2	65.6	70.5	69.7	68.9	68.2	67.5
MTrGO	294.4	281.6	276.1	265.6	256.8	248.8	283.2	265.6	260.1	247.9	243.8

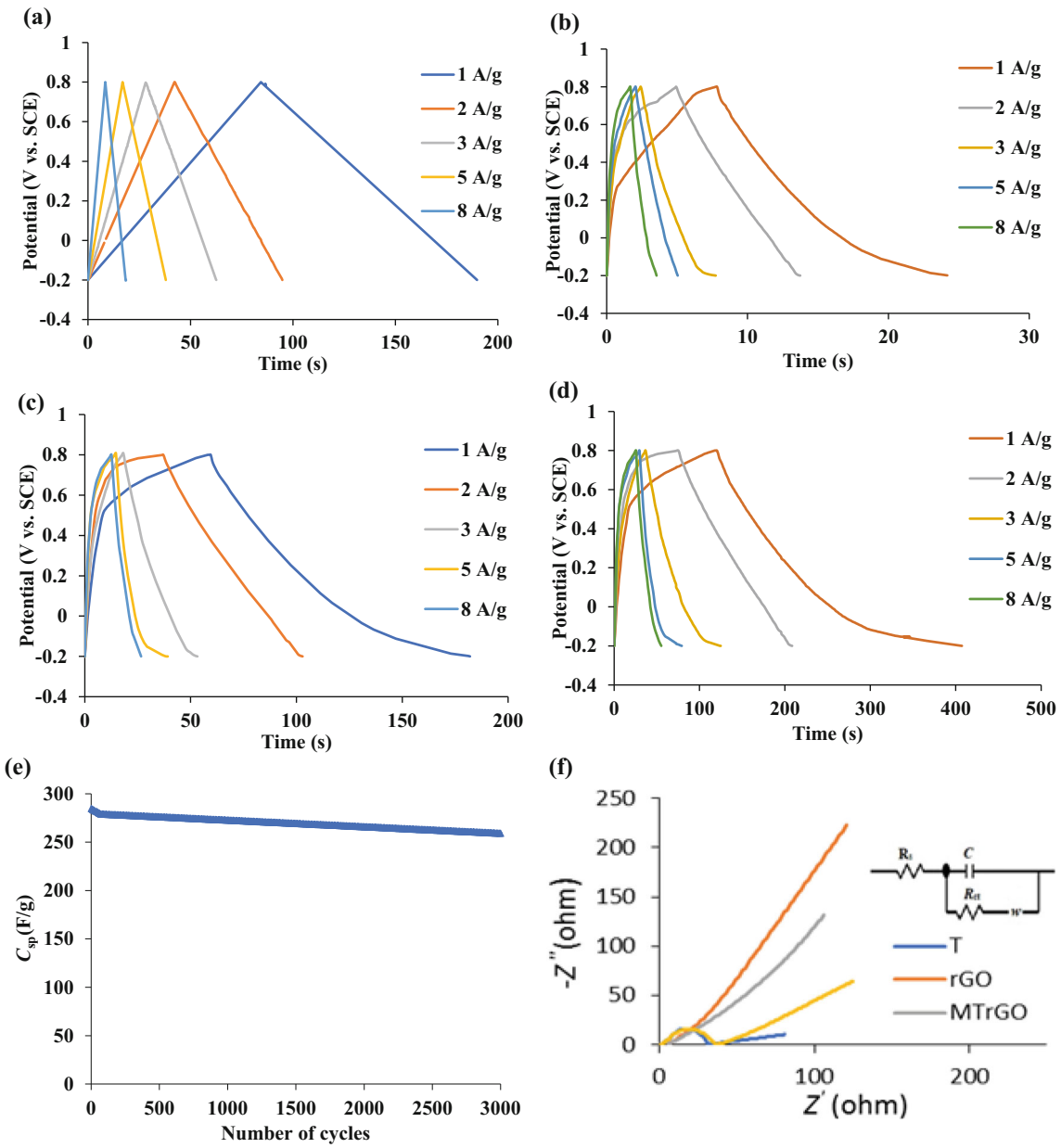

Fig. 8 The GCD curves of **a** rGO, **b** T, **c** M, and **d** MTrGO at different current densities. **e** The cycling stability of MTrGO at a current density of 1 A g^{-1}. **f** The Nyquist impedance plots of rGO, T, M, and MTrGO electrodes and their equivalent electric circuit

The performing in capacitance of ternary materials (Table 3) may be ascribed to the existence of a visible quantity of pleats on the reduced graphene surface intensifies the number of mesopores that can be accessible to K^+ of the electrolyte. Moreover, the high conducting net provided from rGO leads to an improvement in the electron transportation for the period of the charge and discharge progressions, consequently amplifying the electrical properties and charge transfer paths created in pure manganese oxide. The non-rectangular class of the CV plots and the manifestation of peaks at higher scan rates point to departure from the ideal trend and the significant involvement of pseudocapacitance to the total specific capacitance. This performance may be ascribed to that the electrolyte ions do not have sufficient time to insert the deep body of the electrode and created a collection of charge at the interface.

Galvanostatic charging−discharging (GCD) is a corresponding technique for determining the C_{sp} of electrochemical capacitors at constant current. Therefore, the electrochemical presentations of the studied electrodes were also examined by GCD technique at several current densities. All discharge plots (Fig. 8a–d) displayed an internal resistance drop (IR-drop) known as the equivalent series resistance (ESR), which includes all the resistances of the cell (electrode, electrolyte, contact resistance) [52]. More looking at GCD plots shows that

the IR-drop of the ternary electrode is less than those of both TiO_2 and Mn_3O_4 electrodes. This is because the conducting rGO material could work as a speedy electron transportation track in the ternary electrode.

As opposite to rGO, the discharge plots of TiO_2, Mn_3O_4, and ternary composite electrodes reveal a departure from a straight line owing to their pseudocapacitive class.

The specific capacitance values C_{sp} of the electrodes were evaluated from the discharge cycles by using Eq. (5)

$$C_{sp} = \frac{I \times \Delta t}{\Delta V \times m} \tag{5}$$

where I is the response current, Δt is the discharge time, ΔV is the potential range during the charge–discharge measurement, and m is the mass of the active materials on the electrode. The results obtained are given in Table 3, which indicates that all the electrode materials showed a decrease in capacitance with rising in the discharging current rates. This can be explained based on the reduction occurring in the diffusion of electrolyte ions with a time restriction at high scan rates. Just the external active surface can be operated for charge storing, causing a reduction in the electrochemical process of electroactive materials [52, 53]. The results obtained also show that the ternary electrode has the highest capacity value, which can be accredited to the presence of the high conducting rGO in the electrode material besides the synergistic effect produced from the individual materials.

The specific capacitances values obtained from the GCD technique were found to be in good agreement with those obtained from CV measurements. Moreover, the obtained specific capacitance values of Mn_3O_4 are found to be comparable with the previously reported values of nanostructured Mn_3O_4 samples [54, 55].

Long cycling stability is a significant parameter for supercapacitor uses. Thus, the electrochemical stability of the ternary composite electrode (highest C_{sp}) was examined at a current density of 1 A g^{-1}. The outcomes obtained are illustrated in Fig. 8e, which shows that the ternary electrode retained about 91% of its initial capacitance after 3000 cycles and has widespread limited reversibility in successive charge/discharge cycles. The high stability of the composite electrode might be attached to the synergistic effects among the constituents of the ternary system. This could be attributed to that the rGO proceeds some mechanical deformation throughout the redox manner of Mn_3O_4, particles to become more stable by rGO, which operates as a protecting layer; all of these together support in improving the electrochemical stability.

The presence of carbon permitted higher conductivity from carbon pi-electron bonds. Besides, the abundance of oxygen, a highly electronegative element, makes sure that the material is highly conductive. In conclusion, the presence of polar molecules both in rGO, Mn_3O_4, and nanotubes of TiO_2 supported the material to be inertly bonded by strong intermolecular dipole–dipole forces. As a consequence of these properties, improved specific capacitance and minimalized redox reactions were achieved by MTrGO nanocomposite.

Table 4 Parameters values from the fitted impedance equivalent circuit of the investigated electrodes

Sample	RGO	Mn_3O_4	TiO_2	MTrGO
R_s (Ω)	0.18	0.51	0.35	0.28
R_{ct} (Ω)	5.6	35.6	31.5	5.7
W (Ω)	23.1	9.8	5.4	27.5
C_{sp} (F g^{-1})	68	112	17	165

Electrochemical impedance study of positive electrodes

To more understand the electrochemical properties of the investigated electrodes, electrochemical impedance spectroscopy (EIS) was studied. The data obtained helps to quantify electronic and ionic involvements, interfacial capacitance, and surface diffusive behavior in addition to deciding various circuit elements in the bulk electrolyte at the electrode/electrolyte interface. The Nyquist plots of the single and ternary electrodes measured over a frequency range of 10^{-2} to 10^5 Hz are given in Fig. 8f. The figure shows, for each plot, a semicircle in the high-frequency region, Warburg line in the intermediate frequency region, and nearly a vertical line in the low-frequency region. In the high-frequency region, the intercept of the semicircle on the real axis (z') of the Nyquist spectrum represents ESR which specifies the ohmic resistance of the electrolyte, the interfacial contact resistance between current collectors and active materials, and the intrinsic resistance of active materials [56]. The middle-frequency range is related to the electrolyte penetration inside the porous structure of the high porosity electrodes, and this region is usually called the Warburg curve [57]. The slope of the curve in the low-frequency region signifies the resistance that appears during ion diffusion and transport from the electrode to the electrode, and the vertical shape denotes pure capacitive behavior. The diameter of the semicircle represents the area of the reaction site and the sum of the electrolyte resistance (R_s) and the charge transfer resistance (R_{ct}) at the electrode/electrolyte interface. These results indicate that the high-frequency semicircle can be attributed to the charging and discharging process inside the material that corresponds to the charge transfer resistance (R_{ct}) of the electrodes and electrolyte interface [58].

Figure 8 f also shows that the MTrGO electrode exhibits the largest slope at very low frequency, demonstrating that the ternary composite sample is appropriate

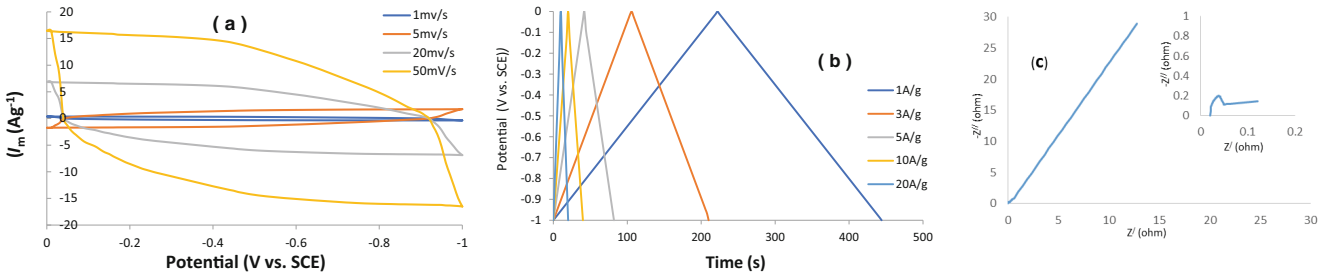

Fig. 9 Electrochemical performance of graphene electrode measured in 6 M KOH solution. **a** The CV curves at different scan rates. **b** The GCD plots at different current densities. **c** The Nyquist impedance plot

to the fast ion diffusion. Thus, it is concluded that the MTrGO supported the charge transfer and ion diffusion due to upgraded electrical conductivity and increased tunnels affected by RGO and the coexistence of Mn and Ti atoms. The Nyquist plots in Fig. 8f were more analyzed by a simulation method using the equivalent circuit shown in the inset of Fig. 8f that composes of R_s (contact resistance), R_{ct} (charge transfer resistance), W (Warburg component), and C (specific capacitance). The fit can perform with errors of less than 5%. The obtained values of fitting parameters of the equivalent circuit are reported in Table 4, which shows that the capacitance value of MTrGO composite is higher than those acquired by their pure components, revealing the synergism of the synthesis method.

To further study the electrochemical performance of the investigated electrodes, the diffusion coefficient of potassium ions in these electrodes is also calculated by the following equation [59]:

$$D^{/\!/} = \frac{R^2 T^2}{2 A^2 n^4 F^2 Ç^2 \sigma^2} \quad (6)$$

where $D^{/\!/}$ represents the diffusion coefficient of K^+ ions, R is the gas constant (8.314 J mol^{-1} K^{-1}), T is the absolute temperature (298.15 K), A is the surface area of the electrode, n is the number of electrons transferred per molecule during K^+ insertion, F is the Faraday constant (96,486 C mol^{-1}), Ç is the potassium-ion concentration, and σ is the Warburg factor, which is associated with the intersection of the straight line on the real axis and can be obtained by the following equation:

$$Z^{/} = R_e + R_{ct} + \sigma\ \omega^{0.5} \quad (7)$$

R_e is the solution resistance, R_{ct} is the charge transfer resistance, and ω is the angular frequency. The calculated potassium ion diffusion coefficient for MTrGO is 3.124×10^{-13} cm^2 s^{-1}, whereas for TiO_2 and Mn_3O_4 electrodes are 2.21×10^{-14} and 1.65×10^{-14} cm^2 s^{-1}, respectively. The increase in the diffusion coefficient of the MTrGO composite than that of its pure constituents may be attributed to its relatively higher pore size and synergetic effect which facilitates the diffusion of electrolyte through the composite electrode.

Electrochemical study of negative electrode

The CV plots of the G sample at different scan rates demonstrate well rectangular shapes without any peaks even at higher scan rates, signifying excellent EDL capacitance behavior (Fig. 9a). The charge–discharge plots at current densities between 1 and 20 A g^{-1}, shown in Fig. 9b, confirm the EDL behavior. The specific capacitances were calculated using Eqs. 2 and 5 and showing values ranging between 204 and 222 F g^{-1} and decrease with increasing each of scan rate and current density. This is due to the agglomeration and restacking of graphene. Figure 7 c is the Nyquist plot of the graphene electrode. The plot shows an arc in the high-frequency section and a spike in the low-frequency region. The small loop area in Fig. 9c represents the dominant resistive nature of the supercapacitor system consisting of electrode/electrolyte/current collector. The start of the arc (left intercept of Z'' at the Z' axis) signifies the resistance (R_s = 0.02 Ω) of the electrolyte in contact with the current collector and electrode. The end of the arc (right intercept of Z'' at the Z' axis) denotes the internal resistance (R_p = 0.05 Ω) of the electrode. The diameter of the arc ($R_p - R_s$ = 0.03 Ω) is equal to the ESR value. The spike in the low-frequency section characterizes the domination of capacitive behavior from the formation of ionic and electronic charges of the electric double-layer system at the pore surfaces; in this region, the ions can more easily diffuse into the pores of graphene [60].

Asymmetric supercapacitor

Because of the high performance of the Mn_3O_4@TiO_2@rGO (MTrGO) ternary composite electrode and in our target to investigate its practical applications, an asymmetric supercapacitor consists of the ternary composite as a positive electrode and G as a negative electrode and PVA–KOH gel electrolyte is studied. The positive electrode of the composite material has oxidation–reduction behavior possessing a high pseudocapacitance, which is useful for enlarging the energy

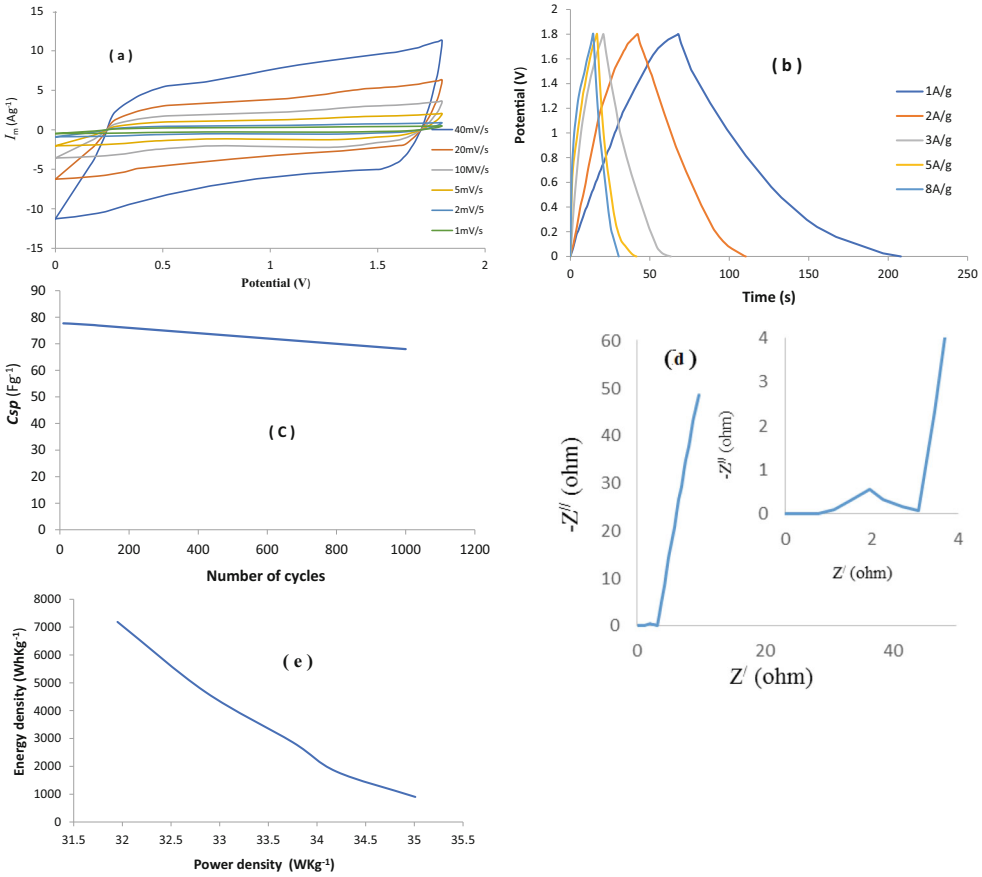

Fig. 10 Electrochemical performance of asymmetric supercapacitor MTrGO//G measured in 6 M KOH solution. **a** The CV curves at different scan rates. **b** The GCD curves at different current densities. **c** The cycling stability. **d** the Nyquist impedance plot. **e** The Ragon plot

density of the asymmetric device, whereas graphene, as a negative electrode, exhibits rich pore size and large specific surface area, which can accumulate charges throughout an electrostatic adsorbing–desorbing manner on the electrode surface. This is favorable to the rapid insertion and extraction of electrolyte ions for developing the power density of the device.

Comparing the CV curves of the positive and negative (G) electrodes in a three-electrode system (Figs. 7e and 9a) shows that the potential difference between the two electrodes is 1.8 V, and thus, the assembled ASC was tested throughout a voltage window of 1.8 V. Moreover, to get maximal cell operating voltage, the packing active mass of the positive and negative electrodes was balanced. The packing mass ratio between the two electrodes was evaluated according to the following equation [61]:

$m+/m- = (C- \times \Delta V-) / (C+ \times \Delta V+)$ in which $m+/m-$, $C+/C-$, and $V+/V-$ are the mass, specific capacitance, and potential windows for the cathode (+)/anode (−), respectively.

Figure 10 a shows the CV curves of the ASC device within a potential window of 1.8 V and sweep rates of 1–40 mV s^{-1}. The figure shows that the assembled ASC revealed a stable capacitive behavior and the CV curves do not show obvious polarization even when the voltage window extended to 1.8 V. This refers to a high tolerance for quick charging/discharging process.

The specific capacitance of the ASC cell is calculated from a CV curve according to Eq. (8) [45, 62].

$$C_{\text{cell}} = \frac{\int_{V-}^{V+} I(V)\mathrm{d}V}{2M \nu V} \tag{8}$$

where C_{cell} (in F g^{-1}) is the specific capacitance of the cell obtained by integrating the positive and negative sweeps in a CV curve, M (in grams, g) is the mass of the active materials in the two electrodes, ν (in V s^{-1}) is the scan rate, and $V = V^{+} - V^{-}$ is the potential window between the

Table 5 Asymmetric cell capacitance of MTrGO/G cell in 6 M KOH at different CV scan rates and different discharging current densities

Scan rate (mV s^{-1})	C_{cell} (F g^{-1})	Current density (A g^{-1})	C_{cell} (F g^{-1})
1.0	81.1	*1.0*	77.5
2.0	78.5	*2.0*	76.1
5.0	74.4	*3.0*	72.6
10.0	70.1	*5.0*	67.6
20.0	66.5	*8.0*	64.5
40.0	64.3		

positive (V^+) and negative (V^-) electrodes. The results obtained are listed in Table 5.

To more evaluate the functioning of the ASC, GCD under different current densities were studied. The plots obtained are represented in Fig. 10b. All curves exhibited small voltage (IR) drop, signifying good reversibility with small internal resistance. Capacitances were evaluated from each discharge curve according to Eq. (9) [62].

$$C_{\text{cell}} = \frac{I}{M} \times \frac{\mathrm{d}V}{\mathrm{d}t} \tag{9}$$

where I is the discharge current, M is the whole mass of the active materials in both electrodes, and $\mathrm{d}V/\mathrm{d}t$ is the slope of the discharge curve. The results obtained are given in Table 5. It is seen that the ASC cells showed good rate performance with not more than 88.5% of capacitance saved when the current density enlarged from 1 to 8 A g^{-1}. This can be attributed to the unique nanostructure with high surface area and high electrical conductivity of G. Plentiful adsorption of ions in addition to an effective ion intercalation/deintercalation and charge transport promoted the good rate capability.

The long-term cycling stability of the ASC is examined at a current density of 1 A g^{-1}, and the obtained results are illustrated in Fig. 10c. It shows high stability for the device, whereas the cell only looses 12.6% of its initial capacitance value after 1000 cycles.

To study the electron and ion diffusion behavior for the duration of the charge−discharge process, EIS of the ASC was measured at frequencies from 10^{-2} to 10^5 Hz and the Nyquist plot is shown in Fig. 10d. The plot demonstrates a typical capacitive shape with a small arc at the high-frequency section and a nearly vertical line in the low-frequency area which demonstrates a pure capacitive behavior of the asymmetric device. The Nyquist plot was analyzed by a simulation method using the equivalent circuit shown in Fig. 8f. The obtained values of fitting parameters of the equivalent circuit are found to be 1.125, 1.195, and 1.711 Ω for contact resistance (R_s), charge transfer resistance (R_{ct}), and Warburg component (W), respectively, and a capacitance of 289 F g^{-1}. The capacitance value of MTrGO composite is higher than those obtained by their pure components, revealing the synergism of the synthesis method.

The energy density (E_d) and average power density (P_d) are two important parameters for the supercapacitor device. They can be calculated from the GCD curve using Eqs. (10) and (11), respectively [63]:

$$E_d = \frac{C_{\text{cell}\ (\Delta V)^2}}{7.2} \tag{10}$$

$$P_d = \frac{3600\ E_d}{\Delta t} \tag{11}$$

where C_{cell} is the cell capacitance, ΔV is the voltage during the discharge process, and Δt is the discharge time. The energy densities of the ASC at various power densities (Ragon plots) of the investigated device are shown in Fig. 10e. It shows an energy density of 31.95 Wh kg^{-1} at the power density of 7188 W kg^{-1}. This reveals that the ternary (MTrGO) composite electrode is a very hopeful material for the electrochemical capacitor with both high-energy and power densities.

Conclusions

In summary, Mn_3O_4, TiO_2, rGO, G, and ternary Mn_3O_4/TiO_2/rGO (MTrGO) nanocomposite are synthesized and characterized via simple, eco-friendly, and low-cost methods and investigated as potential materials for supercapacitor electrodes. The physical characterizations showed that the as-synthesized materials are formed in different morphological structures (fibers for G and rGO, nanotubes for TiO_2, and deformed spherical for Mn_3O_4 and composite), and all of them possess the mesoporous structure. In MTrGO, the rGO sheets act as the platform for even distribution of TiO_2 and Mn_3O_4 nanoparticles; the metal oxides act as the spacer to prevent rGO sheets from stacking. Such a structure offers a high electroactive surface area in which develops the diffusion of the ions within the MTrGO and contributes to huge diffusive charge storage. The MTrGO composite electrode exhibits higher capacitance than its virgin constituent. It has a capacitance of 283.2 F g^{-1} at the current density of 1 A g^{-1} and displayed remarkable cyclic stability. The ASC composing of G negative and MTrGO positive electrodes achieved a relatively high-energy density of 31.95 Wh kg^{-1} and a power density of 7.19 kW kg^{-1} with excellent cycle stability (keeps 87 capacitance retention after 1000 cycles). These results validate that the ternary nanocomposite of MTrGO (cheap material) with porous structure has a promising application in energy storage devices.

References

1. Aray A, Sharma AL (2019) J Solid State Electrochem 23(4):997–1059
2. Kubota K, Kumakura S, Yoda Y, Kuroki K, Komab S (2017) Adv Energy Mater. https://doi.org/10.1002/aenm.201703415 Wiley on Line
3. Maile NC et al (2019) J Mater Sci Mater Electron 30:5555–5566
4. Libich J, Máca J, Vondrák J, Čech O, MSedlaříková M (2018) J Energy Storage 17:224–227
5. Ma Y, Zha M, Dong Y, Li L, Hu G (2019) Mater Res Expr 6(11):6. https://doi.org/10.1088/2053-1591/ab45bd
6. Najib S, Erdem E (2019) Nanoscale Adv 1(8):2817–2827

7. Yadav HM, Ghodake GS, Kim DY, Ramesh S, Maile NC, Lee DS, Shinde SK (2019) Colloids Surf 184 184:110500
8. Shinde SK, Jalak MB, Kim SY, Yadav HM, Ghodake GS, Kadam AA, Kim DY (2018) Ceram Int 44(18):23102–23108
9. Shinde SK, Mohite SM, Kadam AA, Yadav HM, Ghodake GS, Rajpure KY, Lee DS, Kim DY (2019) J Electroanalyt Chem 850: 113433
10. Bryan AM, Santino LM, Lu Y, Acharya S, D'Arcy JM (2016) Chem Mater 28(17):5989–5998
11. Hao X, Zhao J, Li Y, Zhao Y, Ma D, Li L (2011) Colloid Surf Physicochem Eng Aspect 374(1-3):42–47
12. Zhou T, Mo S, Zhou S, Zou W, Liu Y, Yuan D (2011) J Mater Sci 46(10):3337–3342
13. Zhang X, Yu P, Zhang D, Zhang H, Sun X, Ma Y (2013) Mater Lett 92:401–404
14. Zhang X, Sun X, Chen Y, Zhang D, Ma Y (2012) Mater Lett 68: 336–339
15. Sobaszek M, Siuzdak K, Sawczak M, Ryl J, Bogdanowicz R (2016) Thin Solid Films 601(Supplement C):35–40
16. Zhou M, Glushenkov AM, Kartachova O, Li Y, Chen Y (2015) J ElectrochemSoc 162(5):A5065–A5069
17. Salari M, Aboutalebi SH, Chidembo AT, Nevirkovets IP, Konstantinov K, Liu HK (2012) Phys Chem Chem Phys 14(14): 4770–4779
18. Wang T, Peng Z, Wang Y, Tang J, Zheng G (2013) Sci Rep 3:1–9
19. Tang H, Sui Y, Zhu X, Bao Z (2015) Nanoscale Res Lett 10(1): 260–270
20. Yan J, Fan Z, Sun W, Ning G, Wei T, Zhang Q, Zhang R, Zhi L, Wei F (2012) Adv Funct Mater 22(12):2632–2641
21. Hulicova J, Puziy A, Poddubnaya O, Suarez G, Juan M, Lu G (2009) J Am Chem Soc 131:5026–5027
22. Futaba D, Hata K, Yamada T, Hiraoka T, Hayamizu Y, Kakudate Y, Tanaike O, Hatori H, Yumura M, Iijima S (2006) Nat Mater 12: 987–994
23. An Z (2020) Materials 13:716. https://doi.org/10.3390/ma13030716
24. Sing KSW et al (1985) Pure and Appl Chem 5:603–619
25. Kruk M, Jaroniec M (2001) Chem Mater 13(10):3169–3183
26. Wickramaratne NP (2014) Ph. D. Thesis, Kent State University, USA
27. Guerra E, Shanmugharaj A, Choi W, Ryu S (2013) Appl Catal A 468:467–474
28. Sheshmani S, Fashapoyeh M (2013) J Acta Chim Slov 60:813–822
29. Alam S, Sharma N, Kumar L (2017) Graphene 6(01):1–18
30. Perez A, Saja J, Manchado A (2008) J Mater Chem 18:2221–2226
31. Qiu S, Kalita S (2006) Mater Sci Engin A 435-436:327–332
32. Guo H, Wang X, Qian Q, Wang F, Xia X (2009) ACS Nano 3(9): 2653–2659
33. Park S, An J, Potts JR, Velamakanni A, Murali S, Ruoff R (2011) Carbon 49(9):3019–3023
34. Jeong HK et al (2008) J Am Chem Soc 130:1362–1366
35. Wu Z, Ren W, Wen L, Gao L, Zhao J, Chen Z, Zhou G, Li F, Cheng H (2010) ACS Nano 4(6):3187–3194
36. Petit C, Seredych M, Bandosz TJ (2009) J Mater Chem 19(48): 9176–9185
37. Fan X, Yu C, Yang J, Ling Z, Qiu J (2014) Carbon 70:130–141
38. Tiekun J, Fang F, Dongsheng Y, Jianliang C, Guang S (2018) Appl Surf Sci 430:438–447
39. Zhang W, Liu F, Li Q, Shou Q, Cheng J, Zhang L, Nelson BJ, Zhang X (2012) Phys Chem Chem Phys 14(47):16331–16337
40. Oku M, Hirokawa K, Ikeda S (1975) J Electron Spectrosc 7:465473
41. Li Y, Qu J, Gao F, Lv S, Lin S, He C, Sun J (2015) Appl Catal B 162:268–274
42. Sun H, Bai Y, Cheng Y, Jin W, Xu N (2006) Ind Eng Chem Res 45(14):4971–4976
43. Li W, Lei L, Zhao D (2016) Nature Rev Mater 1(6):16023
44. Tan YH (2012) J Mater Chem 22(14):6733–6745
45. Li H, Wang J, Chu Q, Wang Z, Zhang F, Wang S (2009) J Power Sources 190:578–586
46. Selvan R, Perelshtein I, Perkas N, Gedanken A (2008) J Phys Chem C 112(6):1825–1830
47. He L, Zhang G, Dong Y, Zhang Z, Xue S, Jiang X (2014) Nano-Micro Lett 6:38–45
48. Nagamuthu S, Vijayakumar S, Muralidharan G (2013) Energy and Fuels 27(6):3508–3515
49. Wang Y, Li H, Xia Y (2006) Adv Mater 18:2619–2623
50. Du X, Guo P, Song H, Chen X (2010) Electrochim Acta 55(16): 4812–4819
51. Farma R, Deraman M, Awitdrus I, Talib I, Omar R, Manjunatha J, Ishak M, Basri N, Dolah B (2013) Int J Electrochem Sci 8:257–273
52. Jiang T, Chen H, Wan H, Miao L, Zhang L (2013) Electrochim Acta 114:674–680
53. Farsi H, Gobal F, Barzgari Z (2013) Ionics 19(2):287–294
54. Shah H et al (2016) Int J Electrochem Sci 11:8155–8162
55. Shaik D, Rosaiah P, Hussain O (2016) Mater Proceed 3:64–73
56. Mei BA, Munteshari O, Lau J, Dunn B, Pilon L (2018) J Phys Chem C 122(1):194–206
57. Choi W, Shin HC, Kim JM, Choi JY, Yoon WS (2020) J Electrochem Sci Technol 11(1):1–13
58. Wang W, Yao W, Chen W, Chen D, Ma Z, Lu Z (2020) Appl Sci 10(6):1907. https://doi.org/10.3390/app10061907
59. Bard AJ, Faulkner LR (2001) Electrochemical Methods, 2nd edn. Wiley, New Jersey, American
60. Lyu J et al (2019) ChemRxiv. https://doi.org/10.26434/chemrxiv.7637030.V1
61. Shasha J, Tiehu L, Xiong C, Tang C, Dang A, Li H, Zhao T (2019) Nanomaterials 9:1338–1350
62. Sun M, Tie J, Cheng G, Lin T, Peng S, Deng F, Ye F, Yu L (2015) Mater Chem A 3:1730–1736
63. Mousa M, Khairy M, Shehab M (2017) J Solid State Electrochem 21(4):995–1000